



Direct measurement of through-plane thermal conductivity of partially saturated fuel cell diffusion media



G. Xu^a, J.M. LaManna^a, J.T. Clement^a, M.M. Mench^{a,b,*}

^aElectrochemical Energy Storage and Conversion Laboratory, Department of Mechanical, Aerospace and Biomedical Engineering, University of Tennessee, Knoxville, TN 37996, USA

^bEnergy and Transportation Science Division, Oak Ridge National Laboratory, Oak Ridge, TN 37931, USA

HIGHLIGHTS

- Stress–strain relationship was measured to determine thickness and porosity of DM.
- Thermal conductivity was found highly dependent on compression and water content.
- Theoretical prediction of the maximum thermal conductivity was developed.
- Internal cell temperature difference was estimated as a function of saturation.
- PCI flow is more influential on multiphase transport with DM at lower saturation.

ARTICLE INFO

Article history:

Received 23 September 2013

Received in revised form

22 December 2013

Accepted 3 January 2014

Available online 11 January 2014

Keywords:

Thermal conductivity

Diffusion media

Polymer electrolyte fuel cell (PEFC)

Saturation

Microporous layer (MPL)

Heat transfer

ABSTRACT

An experimental study to investigate the through-plane thermal conductivity of three different diffusion media (DM) used in polymer electrolyte fuel cells (PEFCs) as a function of compression (from 0.1 MPa to 2 MPa) and saturation (from 0 to 25%) was performed. Additionally, measurements to determine the stress–strain relationship for the materials were made using an optical microscope. Both compression and water content had a significant impact on the through-plane thermal conductivity, which should be accounted for in multiphase modeling efforts. An analytical expression for the theoretical maximum of the through-plane thermal conductivity, as a function of both compression and saturation, was developed to help understand the nature of liquid connectivity in saturated pores. Additionally, a relationship was developed to predict actual thermal conductivity of the tested materials as a function of both compression and saturation based on experimentally measured data.

© 2014 Elsevier B.V. All rights reserved.

1. Introduction

Carbon paper is used as the diffusion medium (DM) in polymer electrolyte fuel cells (PEFCs) due to its suitable permeability, electronic conductivity, thermal conductivity, and mechanical strength. Thermal conductivity is a particularly important parameter, due to the interplay between heat and water management [1–4] and the perceived dominance of conduction heat transfer in PEFCs. Water generated in PEFCs that condenses into liquid phase must be removed to prevent loss of performance during operation and potential freeze–thaw degradation [5–8]. Polytetrafluoroethylene

(PTFE) is normally used to improve hydrophobicity of the DM and reduce liquid accumulation. A highly hydrophobic microporous layer (MPL) is often utilized between the DM and catalyst layer (CL). The MPL is of great importance to mitigate flooding, to decrease electrical contact resistance, protect the membrane from damage from DM fibers, and prevent dryout from excessive vapor removal.

Various experimental approaches have been employed to measure the thermal conductivity of unsaturated DM [9–14]. Khandelwal and Mench [11] measured carbon paper and Nafion® membranes for PEFCs. They reported that Sigracet® 20 wt.% PTFE treated carbon paper had a thermal conductivity of $0.22 \pm 0.04 \text{ W m}^{-1} \text{ K}^{-1}$ and Toray paper had a thermal conductivity of $1.80 \pm 0.27 \text{ W m}^{-1} \text{ K}^{-1}$. Burheim et al. [12] reported an increase of thermal conductivity of artificially aged SGL gas diffusion media while PTFE content decreases. They also measured SolviCore DM at different compression pressures. They reported that thermal

* Corresponding author. Energy and Transportation Science Division, Oak Ridge National Laboratory, Oak Ridge, TN 37931, USA. Tel.: +1 865 974 6751; fax: +1 865 974 5274.

E-mail address: mmench@utk.edu (M.M. Mench).

conductivity increases as compression pressures grow and an increase in thermal conductivity when the DM is saturated [13]. Zamel et al. [9] measured the through-plane thermal conductivity of unsaturated Toray paper in a temperature range from -50°C to 120°C . A thermal conductivity of $0.8\text{--}1.8\text{ W m}^{-1}\text{ K}^{-1}$ was reported at high compression, and $0.2\text{--}0.4\text{ W m}^{-1}\text{ K}^{-1}$ at low compression. Although measurement of dry media is useful, in operation, PEFCs commonly have DM saturation at levels up to 30% [15–17]. Therefore, knowledge of partially saturated conductivity is important.

Several researchers also proposed numerical models to calculate thermal conductivity of DM [18–20]. In order to better understand the mechanism of water transport and its effect on performance and durability, Bazylak provided an overview of recent developments in liquid water visualization with PEFCs [21]. Yablecki et al. [22] reported an increase of 20.8% in through-plane thermal conductivity for their gas diffusion layer (GDL) modeling domain with 24.4% saturation. However, measurement of the thermal conductivity of diffusion media as a function of both compression and a full range of saturation has not yet been fully developed, so that the impact on transport can be fully understood, which is the motivation for this study. In this work, measurements of stress–strain relationship and thermal conductivity as a function of saturation were performed. A theoretical analysis of the maximum thermal conductivity as a function of saturation has been developed to glean insight into the internal distribution and connectivity of liquid in the media. Water transport within the saturated DM was also investigated via calculations of phase-changed-induced (PCI) flow and its impact as a function of saturation [23]. The results of this work should be useful to understand and more precisely model thermal transport in operating PEFCs with realistic saturation distributions.

2. Experimental setup

Diffusion media were uniformly compressed between two 25 mm thick stainless steel cylinders with known thermal conductivity. This design enabled determination of the stress–strain relationship and the through-plane thermal conductivity. Schematic diagrams of the experimental apparatus are shown in Figs. 1 and 2. A load cell was used to measure compression pressure on the diffusion media. All tests were performed at room temperature, which varied from 21°C to 27°C throughout the course of testing.

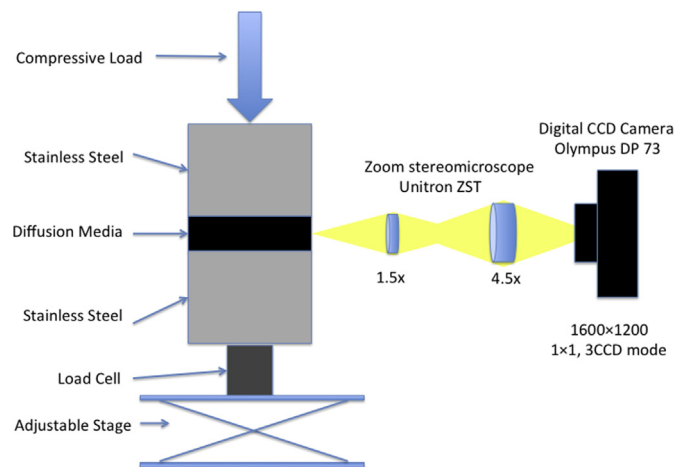


Fig. 1. Schematic diagram of the experimental apparatus used to optically measure stress–strain in thin film materials (not to scale).

3. Design and instrumentation

A Hot Disk TPS2500S Thermal Constants Analyser (Hot Disk AB, Gothenburg, Sweden & ThermTest Inc., Fredericton, Canada) was used to measure the thermal conductivity of all materials tested in this work. Based on the theory of the Hot Disk Transient Plane Source (TPS) technique, a TPS sensor in the shape of a double spiral was utilized to take measurements within ten seconds, effectively decreasing unwanted water vaporization during the tests. The TPS sensor acted both as a heat source for increasing the temperature of the samples and a resistance thermometer for recording the time dependent temperature increases [24]. The reproducibility of measured thermal conductivity using this technique was observed to be $\pm 3\%$. A TPS 7280 thin film sensor with a sensor diameter of 29.34 mm was used for all testing. This large format sensor provides a uniform heat flux across the measurement area.

4. Measurement and uncertainty analysis

Round, 53 mm diameter samples were used for stress–strain measurement. Mitsubishi Rayon Corp. Grafil U-105 (MRC 105), SGL Sigracet® 25 BC, and General Motors (GM) Experimental virgin samples were used in this study. GM Experimental samples are materials that satisfy the 2015 US DOE performance targets while enabling progress toward the automotive fuel cell system cost target of $\$30/\text{kWe}$ as developed under DOE Award Number DE-EE0000470. To reduce measurement error, two samples of MRC 105, SGL 25 BC, or GM Experimental were layered for each stress–strain measurement. Images of compressed samples were captured using a zoom stereomicroscope (Unitron ZST) and digital CCD camera (Olympus DP 73) with optical resolution of 1600×1200 pixels. Deflections of the DM in the images were measured using digital imaging software cellSens Standard.

In this study, the DM stress–strain relationship was optically measured, as shown in Fig. 3. The thickness versus compression relationship was then used to calculate the thickness used in the determination of compressed DM thermal conductivity. Porosity is of great importance to calculate the actual saturation of the porous media. As compression increases, the void volume in DM is reduced, decreasing effective porosity according to the following equation:

$$\phi^* = 1 - \frac{1 - \phi}{1 - \varepsilon} \quad (1)$$

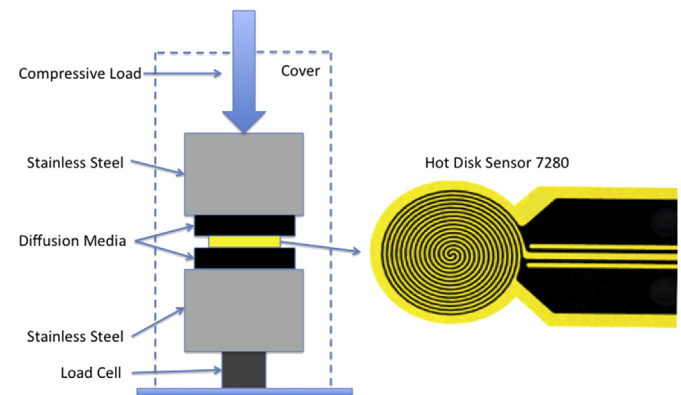


Fig. 2. Schematic diagram of the experimental apparatus used to measure thermal conductivity of thin film materials (not to scale).

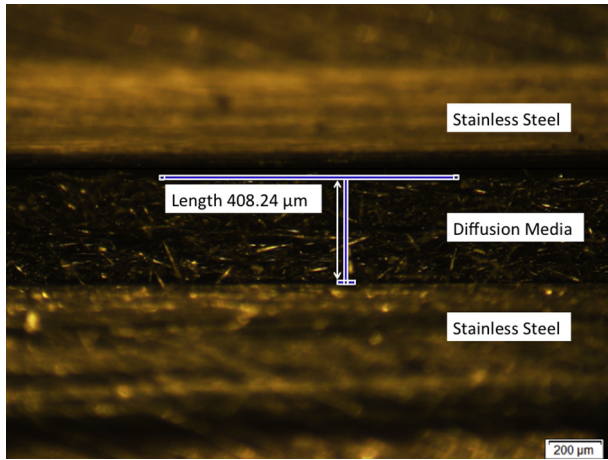


Fig. 3. Micrograph of a DM under compression.

where ϕ^* is the compressed porosity of DM, ϕ is the initial porosity of DM, and ε is the total strain on the compressed DM. It should be noted that during compression to 2 MPa, the MPL is essentially incompressible when layered as a composite with the much less stiff diffusion media, so that the load deformation can be considered on the DM only. Table 1 shows initial porosity and compressed porosity of three different diffusion media at compression of 2 MPa.

4.1. Saturation of the DM

Unsaturated weight and thickness were measured prior to the saturation process using a Sartorius TE214S analytical balance. In this study, porous diffusion media were artificially saturated by immersion in de-ionized (DI) water in a sealed container while a vacuum was applied. A sonic bath was utilized to remove residual bubbles during immersion and saturation [25].

The thickness at compression of 2 MPa was calculated based on the stress strain relationship and the following equation:

$$l = l_0 \frac{1 - \varepsilon}{1 - \varepsilon^0} \quad (2)$$

where l is the thickness of compressed DM, l_0 is the thickness of measured DM, ε is the total strain on compressed DM, ε^0 is the strain on measured DM.

The saturated weight of the diffusion medium was calculated prior to saturation based on the following equation:

$$m_{\text{wet}} = m_{\text{dry}} + s \rho_{\text{water}} A l_1 \phi^* \quad (3)$$

where m_{wet} and m_{dry} are weights of saturated and unsaturated diffusion media, respectively, s is the saturation of DM, ρ_{water} is the density of water, A is the area of DM, l_1 is the thickness of the compressed macroporous layer, ϕ^* is the compressed porosity of the DM.

For MRC 105 DM, without MPL, the thickness of the DM l_1 is the thickness of compressed DM. For GM Experimental DM shown in Fig. 4, with thin MPL, the thickness of the compressed macroporous

layer was almost the same as the thickness of compressed DM since the MPL is relatively thin compared to the macroporous layer. For SGL 25 BC, with a thicker MPL, the thickness of the compressed macroporous layer was used to calculate saturation instead of the thickness of compressed DM since the highly hydrophobic MPL was assumed to be unsaturated. The compressed porosity of DM was calculated as shown in Table 1.

Since some water can be squeezed out of the diffusion media during compression loading, the average decrease in saturation level during compression loading was calculated and compensated prior to saturation process. After each test series, an updated saturated weight was immediately measured. Saturation was calculated based on the following equation:

$$s = \frac{m_{\text{wet}} - m_{\text{dry}}}{\rho_{\text{water}} A l_1 \phi^*} \quad (4)$$

4.2. Unsaturated and saturated DM thermal conductivity measurement

Thermal conductivity was measured with the through-plane test module. Two specimens were required for each test. As shown in Fig. 2, one sample was placed above the Hot Disk sensor. The other was placed underneath the sensor. The assembly was firmly clamped between two 25 mm thick stainless steel cylinders with known high thermal conductivity. Samples were consecutively tested at compressions of 0.1 MPa, 0.5 MPa, 1 MPa, 1.5 MPa and 2 MPa. Thirty minutes of pre-test time was taken before each test to ensure steady state conditions. The actual measurement time was 10 s at a heating power of 2.2 W. The ambient temperature in this study varied from 21 °C to 27 °C, which should not make a significant impact on results based on previous studies [11].

In the experiments for determination of saturated DM thermal conductivity, the compression pressure was set at 2 MPa, which is within the normal range for a fuel cell assembly. Samples were initially saturated to a high saturation level and allowed to evaporatively dry until the target saturation level was reached.

4.3. Measurement validation

The thickness measurement was validated with a stage micrometer for transmitted light (Ted Pella, Inc.). The measured thickness was 1.89% lower than the actual value, which is within the expected experimental uncertainty.

Thermal measurement was validated with a thin disk of Teflon® PTFE, SGL 25 BC DM and stainless steel. The measured PTFE thermal conductivity was determined to be $0.240 \pm 0.025 \text{ W m}^{-1} \text{ K}^{-1}$ compared to the Teflon® PTFE standard thermal conductivity of $0.259 \pm 0.006 \text{ W m}^{-1} \text{ K}^{-1}$. The measured SGL 25 BC thermal conductivity was $0.214 \pm 0.004 \text{ W m}^{-1} \text{ K}^{-1}$ at compression of 0.5 MPa and $0.356 \pm 0.018 \text{ W m}^{-1} \text{ K}^{-1}$ at compression of 1 MPa. Ramousse et al. [26] reported a thermal conductivity of $0.26\text{--}0.34 \text{ W m}^{-1} \text{ K}^{-1}$. Khandelwal and Mench [11] reported thermal conductivity of $0.31 \pm 0.06 \text{ W m}^{-1} \text{ K}^{-1}$. The measured stainless steel thermal conductivity was $13.380 \pm 0.036 \text{ W m}^{-1} \text{ K}^{-1}$. Hot Disk AB, a Sweden company which develops, designs, manufactures, sells, installs and services Thermal Constants Analyzer, reported an average thermal conductivity of $13.7418 \text{ W m}^{-1} \text{ K}^{-1}$ with less than 0.15% standard deviation based on these results, the test system was deemed to be within acceptable limits of accuracy [27].

Table 1
Calculated change in porosity at compression of 2 MPa.

| DM | Initial porosity | Compressed porosity |
|-----------|------------------|---------------------|
| GM Exp. | 82.0% | 67.8% ± 1.2% |
| SGL 25 BC | 80.0% | 64.8% ± 0.7% |
| MRC 105 | 83.2% | 79.1% ± 0.2% |

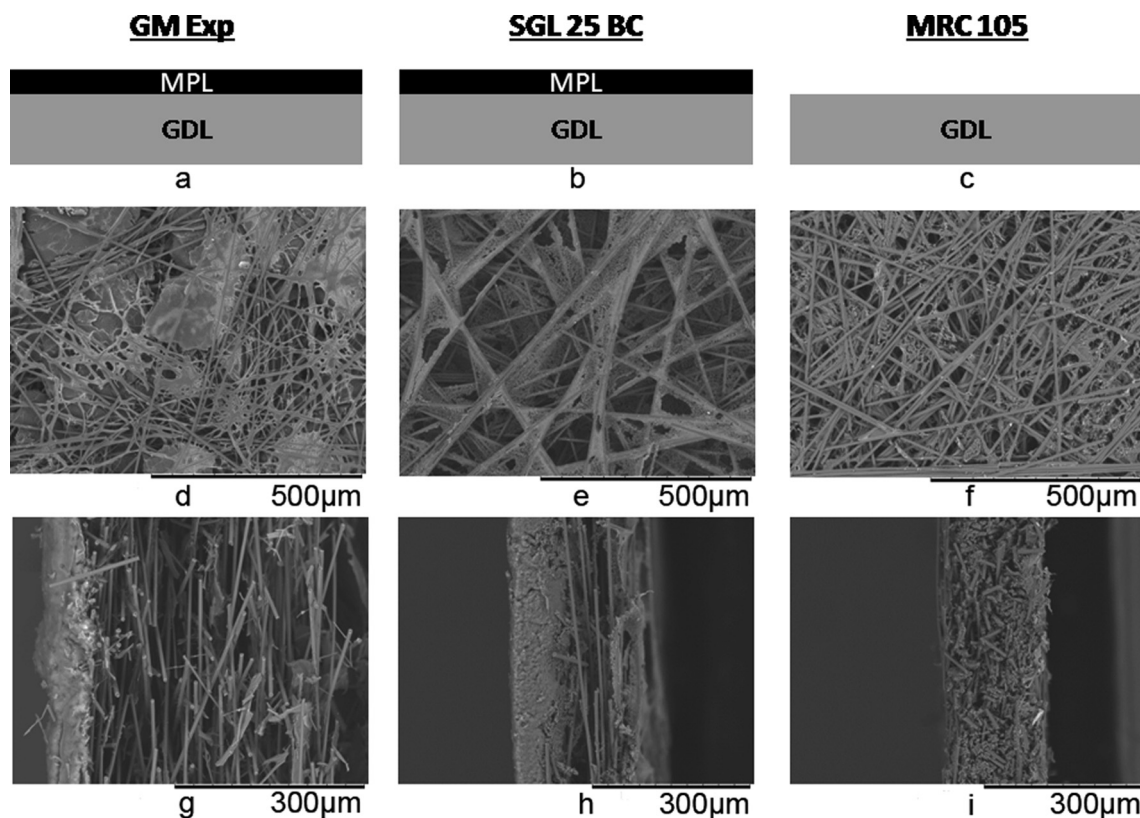


Fig. 4. Configuration of DM a) GM Exp. MPL coated on GDL b) SGL 25 BC MPL coated on GDL c) MRC 105 GDL without MPL coating d) GM Exp. face of macroporous layer e) SGL 25 BC face of macroporous layer f) MRC 105 face of macroporous layer g) GM Exp. cross section h) SGL 25 BC cross section i) MRC 105 cross section.

5. Results and discussion

5.1. SEM images

The characteristic structures of the cross-section, the face of the macroporous layers and the face of the microporous layers are shown in Fig. 4 using scanning electron micrographs (HITACHI TM3000).

The micrographs show that SGL 25 BC, MRC 105 and GM Experimental DM primarily have planar structures of fibers aligned in multiple layers. The presence of PTFE can be observed between the fibers. SGL 25 BC has a relatively thick MPL (46% of DM

thickness), which is essentially incompressible under the loads in testing. The GM Experimental samples have a much thinner MPL, and the MRC 105 samples do not have a MPL. In the GM Experimental DM, a carbon-fiber skeleton filled with carbon powder is observed, as shown in Fig. 4.

5.2. Stress–strain relationship

Fig. 5 presents three fitting curves of the measured stress–strain deflection for GM Experimental, SGL 25 BC and MRC 105. The stress–strain relationship for the DM is essential to adjust for thermal conductivity measurements for actual thickness. For GM Experimental DM, the strain sharply increases 15% during initial compression loading (0.1 MPa) and nonlinearly approaches 44% at compression of 2 MPa. The effective compressed porosity is reduced from 82.0% to 67.8% during compression to 2 MPa. For SGL 25 BC MPL, the total strain is calculated to be 4.9%. For SGL 25 BC macroporous layer, the strain reaches 10% during the initial compression loading, and approaches 31% resulting in reduced porosity from 80.0% to 64.8%. MRC 105 samples do not have as much strain during the initial compression loading. Following a 9% strain at compression of 0.25 MPa, MRC 105 samples deflect linearly up to 19.5% at compression of 2 MPa. A nonlinear curve fitting was performed using an exponential association model:

Table 2
Measured stress–strain curve fit functions.

| DM | Experimental stress–strain curve fit functions |
|-----------|--|
| GM Exp. | $\epsilon = 0.14429(1 - e^{-\sigma/0.04031}) + 0.31607(1 - e^{-\sigma/0.70534})$ |
| SGL 25 BC | $\epsilon = 0.29558(1 - e^{-\sigma/1.68126}) + 0.10073(1 - e^{-\sigma/0.02651})$ |
| MRC 105 | $\epsilon = 0.07055(1 - e^{-\sigma/0.12226}) + 1.79812 \cdot 10^8(1 - e^{-\sigma/2.98335 \cdot 10^9})$ |

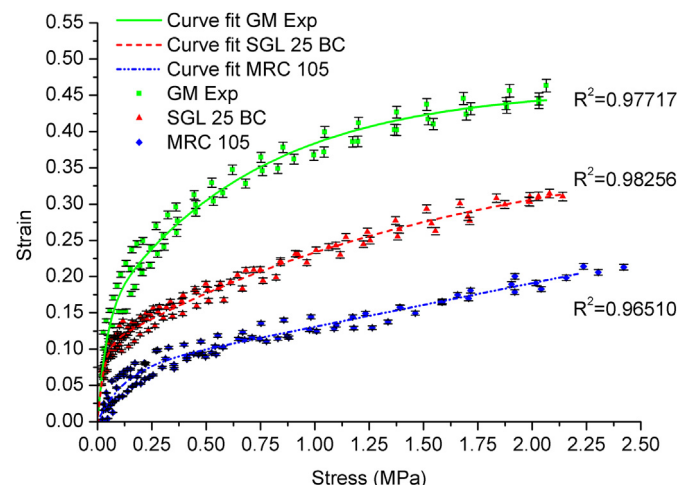


Fig. 5. Experimental data and curve fit lines for measured stress–strain relationships.

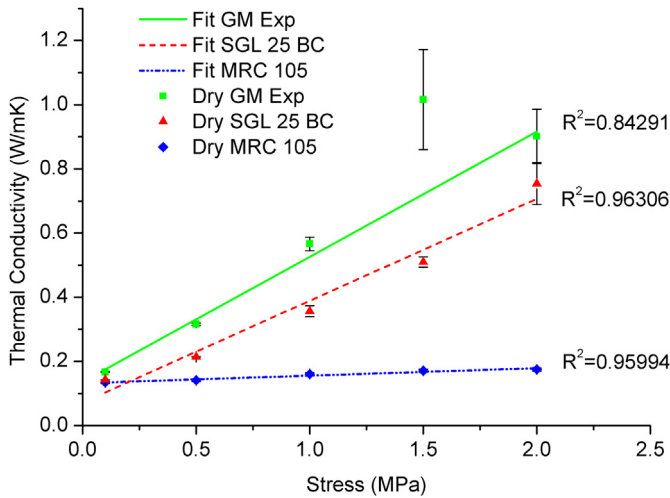


Fig. 6. Measured thermal conductivity of unsaturated DM as a function of compression.

$$Y = a_1 \left(1 - e^{-\frac{x}{b_1}}\right) + a_2 \left(1 - e^{-\frac{x}{b_2}}\right) \quad (5)$$

Table 2 and Fig. 5 show the three experimental stress–strain curve fitting models of GM Experimental, SGL 25 BC and MRC 105, respectively.

A residual strain can be observed when the compressive load is released due to plastic deformation. In this study, the focuses are thickness measurement and prediction, and thermal conductivity measurements were only performed on virgin materials under first compression. Therefore, successive compress–release cycles were not performed.

5.3. Thermal conductivity measurement of unsaturated samples

Fig. 6 and Table 3 show measured thermal conductivity averaged across five tests using material from the same lot to reduce manufacturing variability and linear fitting functions derived from unsaturated DM under various compressions up to 2 MPa. Contact resistance between the samples and the sensor has been removed from the measured data by the device as the influence of contact resistance only occurs during the initial portion of the transient measurement [28,29]. Thermal conductivity was relatively lower when low compression pressure was applied because of the presence of the internal contact resistance and high porosity in the DM. With increased compression, internal contact resistance and porosity decreases, and thermal conductivity increases. The thermal conductivity of unsaturated GM Experimental DM monotonically increases with respect to compression pressure from 0.1 MPa to 2 MPa by 440%. The measured thermal conductivity increased about 80% when compression pressure varied from 1.0 MPa to 1.5 MPa. Since the strain almost reached a maximum, carbon powder and carbon fiber were more connected with each other reducing internal conductive resistance and forming enhanced heat transfer pathways. The thermal conductivity of

Table 3
Measured unsaturated thermal conductivity fit functions.

| DM | Experimental unsaturated thermal conductivity linear fit functions |
|-----------|--|
| GM Exp. | $k_{dry} = 0.136 + 0.390\sigma$ |
| SGL 25 BC | $k_{dry} = 0.07121 + 0.31777\sigma$ |
| MRC 105 | $k_{dry} = 0.13209 + 0.02349\sigma$ |

unsaturated SGL 25 BC and MRC 105 DM linearly increases with respect to compression loading.

5.4. Thermal conductivity measurement of saturated samples

Fig. 7 and Table 4 presents measured thermal conductivity and fit functions of saturated GM Experimental, SGL 25 BC and MRC 105 DM at compression of 2 MPa. As expected, water content has a significant effect on the increment of thermal conductivity of DM since it replaces air. The thermal conductivity of MRC 105 sharply increases nearly 62% from 0 to 6% saturation and gradually approaches theoretical maximum as saturation levels increase. The theoretical maximum shown is developed from a simple analytical model that was derived for comparative purposes only, and is described later in this work. As shown in Fig. 7, water content obtained in GM Experimental samples has an obvious influence on thermal conduction with saturation from 0 to 10%. Similar to MRC 105, the thermal conductivity of SGL 25 BC gradually increases 35% as saturation level increases from 0 to 25%. As saturation increases, the measured thermal conductivity approaches the theoretical maximum thermal conductivity as a function of saturation since more connectivity of solid and liquid components occurs in the compressed DM.

5.5. Prediction of thermal conductivity of saturated samples based on experimentally measured results

Figs. 6 and 7, Tables 3 and 4 show a good agreement on the thermal conductivity of unsaturated DM at compression of 2 MPa. The intercepts of saturated thermal conductivity curve fit functions in Table 4 represents thermal conductivity of unsaturated DM at compression of 2 MPa, which can be substituted by the unsaturated thermal conductivity linear fit functions in Table 3, yielding the prediction of the thermal conductivity of saturated DM as a function of both compression and saturation, which is presented in Table 5.

5.6. Theoretical maximum prediction of thermal conductivity using parallel model and series–parallel model

It is well known that DM used in PEFC is a heterogeneous material with carbon fibers or cloth and heat conduction is a dominant

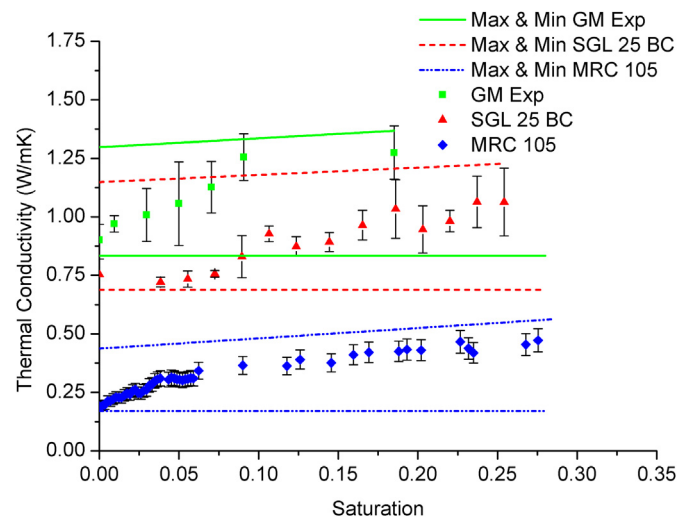


Fig. 7. Measured and predicted maximum and minimum thermal conductivity as a function of saturation for various DM at 2 MPa compression.

Table 4
Measured saturated thermal conductivity fit functions.

| DM | Saturated thermal conductivity curve fit functions |
|-----------|---|
| GM Exp. | $k_{wet} = 0.9071 + 0.44496(1 - e^{-s/0.08874})$ |
| SGL 25 BC | $k_{wet} = 0.70051 + 1.44259s$ |
| MRC 105 | $k_{wet} = 0.1872 + 0.52403(1 - e^{-s/0.6967}) + 0.11151(1 - e^{-s/0.03477})$ |

Table 5
Predicted thermal conductivity of saturated DM as a function of compression and saturation based on experimental measurement.

| DM | Predicted thermal conductivity of saturated DM |
|-----------|--|
| GM Exp. | $k_{wet} = 0.136 + 0.390\sigma + 0.44496(1 - e^{-s/0.08874})$ |
| SGL 25 BC | $k_{wet} = 0.07121 + 0.31777\sigma + 1.44259s$ |
| MRC 105 | $k_{wet} = 0.13209 + 0.02349\sigma + 0.52403(1 - e^{-s/0.6967}) + 0.11151(1 - e^{-s/0.03477})$ |

heat transfer mode through the DM. Many models have been described in literature [18,19,30–33] to predict the thermal conductivity of porous diffusion media. But saturation was not considered in those models, primarily due to lack of experimental data now available.

A simplified model meant only to examine limiting behavior was developed in this study with basic components (carbon, water and air) connected, and parallel to the heat flow, as shown in Fig. 8. This represents the theoretical maximum of thermal conductivity of porous diffusion media at compression of 2 MPa, if all saturation was connected and aligned.

$$k_1 = \phi^*(k_w - k_a)s + (1 - \phi^*)k_c + \phi^*k_a \quad (6)$$

$$k_2 = k_c \quad (7)$$

$$k = \frac{l}{\frac{l_1}{k_1} + \frac{l-l_1}{k_2}} \quad (8)$$

For SGL 25 BC:

$$k = \frac{4.12232s + 8.22939}{s + 8.68781} \quad (9)$$

For MRC 105:

$$k = 0.4398s + 0.437 \quad (10)$$

For GM Experimental:

$$k = 0.376968s + 1.29783 \quad (11)$$

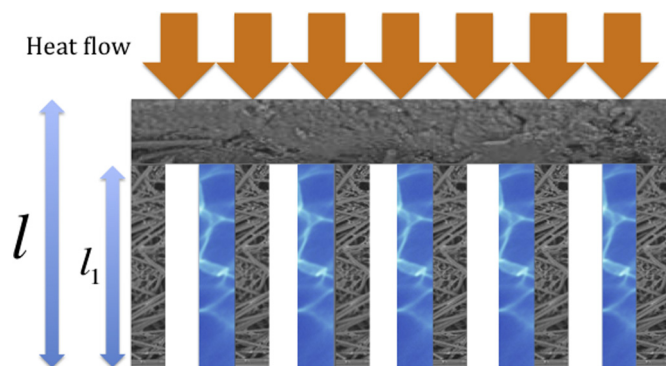


Fig. 8. Illustration of simple model to predict theoretical maximum thermal conductivity of partially saturated porous diffusion media.

where k_w is the thermal conductivity of water, k_c is the thermal conductivity of carbon, k_a is the thermal conductivity of air, l_1 is the thickness of compressed macroporous layer, and l is the thickness of compressed DM.

The theoretical maximum and minimum (i.e. measured dry) prediction of thermal conductivity using this limiting model is presented in Fig. 7. A significant difference between measured unsaturated thermal conductivity and theoretical maximum was observed, since the planar structures of the fibers in all of three DM are orthogonal to the direction of heat flow. At low saturation, water droplets begin to connect along multiple fibers among different sub-layers to create connected heat conduction pathways. These pathways significantly increase thermal conductivity. As saturation increases, multiple pores fill with water forming more connected heat conduction pathways, approaching theoretical limits. The theoretical limit represents a condition in which all water in the diffusion medium is aligned and connected in the direction of heat flow, maximizing conductivity for a given saturation. The fact that the measured curve would fail to completely merge with the maximum is expected, since a certain degree of tortuosity in the DM exists, and the water will not be completely connected.

5.7. Theoretical maximum thermal conductivity as a function of both compression and saturation

The compressed porosity is a function of strain, and strain is a function of compression, therefore compressed porosity can be described as a function of compression.

Substituting Equation (1) in Equation (6) yields:

$$k_1 = \left(1 - \frac{1 - \phi}{1 - \varepsilon^*}\right)[(k_w - k_a)s - k_c + k_a] + k_c \quad (12)$$

For SGL 25 BC material:

$$\phi = 0.800, \quad \frac{l_1}{l} = \frac{1 - \varepsilon^*}{1 - \varepsilon}(1 - 46\%) \quad (13)$$

$$\varepsilon^* = 0.1427\left(1 - e^{-\frac{\sigma}{0.1}}\right) + 1.88643 \times 10^{13}\left(1 - e^{-\frac{\sigma}{1.30697 \times 10^{14}}}\right) \quad (14)$$

For MRC 105 material:

$$\phi = 0.832, \quad l_1 = l, \quad \varepsilon^* = \varepsilon \quad (15)$$

For GM Experimental material:

$$\phi = 0.820, \quad l_1 \approx l, \quad \varepsilon^* = \varepsilon \quad (16)$$

where ε^* is the strain on the macroporous layer, ϕ is the initial porosity of DM.

Substituting Equations (7), (8), (13) and (14) and Table 6 in Equation (12), the theoretical prediction of maximum thermal conductivity for SGL 25 BC was solved:

Table 6
Material properties of DM used in this study.

| DM | ϕ^* (%) | k_w (Wm ⁻¹ K ⁻¹) | k_c (Wm ⁻¹ K ⁻¹) | k_a (Wm ⁻¹ K ⁻¹) | $l_1 l^{-1}$ |
|-----------|-----------------|--|--|--|--------------|
| GM Exp. | 67.8 | 0.58 | 3.98 | 0.024 | ≈ 1 |
| MRC 105 | 79.1 | 0.58 | 1.7 | 0.024 | 1 |
| SGL 25 BC | 64.8 | 0.58 | 1.7 | 0.024 | 0.412 |

*Compressed to 2 MPa.

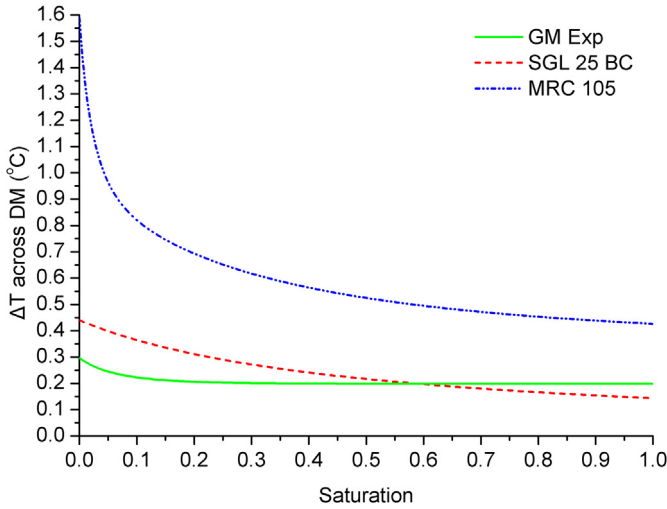


Fig. 9. Estimated temperature difference across a cathode DM in a fuel cell operating at 0.6 V, 1.0 A cm⁻² and 353 K.

$$k = \frac{85(\varepsilon - 1)(695\varepsilon^*s + 30\varepsilon^* - 556s - 449)}{\omega} \quad (17)$$

$$\begin{aligned} \omega = & 106250\varepsilon^2 + 34750\varepsilon\varepsilon^*s - 162125\varepsilon\varepsilon^* - 27800\varepsilon s - 14000\varepsilon \\ & - 18765(\varepsilon^*)^2s + 113940(\varepsilon^*)^2 + 17792\varepsilon^*s - 110980\varepsilon^* \\ & - 2224s + 55575 \end{aligned} \quad (18)$$

Substituting Equations (7), (8) and (15) and Table 6 in Equation (12), the theoretical prediction of maximum thermal conductivity for MRC 105 was solved:

$$\varepsilon = 0.07055 \left(1 - e^{-\frac{\sigma}{0.12226}}\right) + 1.79812 \cdot 10^8 \left(1 - e^{-\frac{\sigma}{2.98335 \cdot 10^9}}\right) \quad (19)$$

Substituting Equations (7), (8) and (16) and Table 6 in Equation (12), the theoretical prediction of maximum of thermal conductivity for GM Experimental was solved:

$$k = \frac{0.556\varepsilon s + 0.024\varepsilon - 0.462592s - 0.73608}{\varepsilon - 1} \quad (20)$$

5.8. The effect of thermal conductivity on multiphase mass transport

It has been shown experimentally as well as numerically that a temperature gradient across diffusion media induces additional water transport due to phase change, this phase-change-induced (PCI) flow has also been referred to as the heat pipe effect [23,34,35]. These effects are significant in terms of the overall water balance of a cell. In order to assess the influence of PCI flow, the developed semi-empirical thermal conductivity relationships were used to calculate a ratio between PCI flow and water generated from the electrochemical reaction. First, a temperature difference across each DM sample was calculated as a function of saturation. Using the cathode catalyst layer heat generation term and Fourier's law of conduction, for a single cell operating at 0.6 V, 1.0 A cm⁻², 353 K, 101 kPa back pressure, the temperature difference across each DM was estimated as a function of saturation. This result, shown in Fig. 9, indicates that saturation must be considered to ensure computational accuracy. Evidently this holds true for cell

heat flux calculations, however, variation in saturation (thus cell temperature gradients) will also influence water management via PCI flow.

Since PCI flow is governed by cell temperature gradients, this relationship was then correlated to a saturation pressure difference [36]. A PCI molar flow rate can be calculated as a function of saturation via an effective vapor diffusion coefficient D_v^{eff} and this saturation pressure difference [23],

$$D_v^{\text{eff}} = D_{v_0} [\phi(1-s)]^{1.5} \left(\frac{T}{T_0}\right)^n \left(\frac{p_0}{p}\right) \quad (21)$$

where D_{v_0} is the diffusivity at absolute temperature T_0 and pressure p_0 with a constant n of 1.81 [37]. The diffusivity D_{v_0} was taken to be $0.226 \cdot 10^{-4} \text{ m}^2 \text{ s}^{-1}$ at 273.15 K and 101 kPa. The PCI molar flux J was then determined using Fick's law for diffusion

$$J = D_v^{\text{eff}} \frac{\partial C}{\partial x} \quad (22)$$

$$C = \frac{P_{\text{sat}}}{RT} \quad (23)$$

where C is the local water concentration, which is a function of the saturation pressure P_{sat} , ideal gas constant R , and temperature T . Under the chosen cell operating conditions, the calculated ratio of PCI molar flow to the molar flow of water generated by reaction was then determined as a function of saturation, as seen in Fig. 10.

The significance of this result is that, at lower saturation, PCI flow is more influential on multiphase transport within fuel cell DM. The results also indicate that thermal resistance plays an integral role in the overall water balance and transport in the cell, which has already been demonstrated in the literature. When this ratio is near unity, it indicates that PCI flow is capable of transferring all water generated within the catalyst layer across the cathode DM, which agrees with the experimental results of Owejan et al. [38]. Thus, in order to properly account for these transport effects on overall water balance, more precise thermal conductivity variations must be considered for accurate prediction.

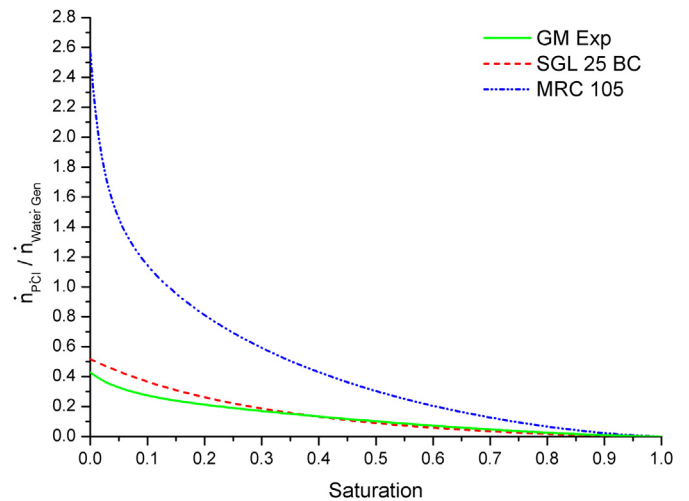


Fig. 10. Ratio of PCI molar flow rate to molar rate of water generated in a fuel cell operating at 0.6 V, 1.0 A cm⁻², 353 K and 101 kPa.

6. Conclusions

The relationship between thermal conductivity and both compression and saturation in three representative fuel cell diffusion media was investigated. Additionally, the stress–strain relationships of the materials were measured using an optical microscopic technique. The through-plane thermal conductivity of diffusion media was found to be highly dependent on the compression and the water content, and expressions relating saturation and compression to thermal conductivity were developed. Additionally, a theoretical prediction of the maximum through-plane thermal conductivity was developed as a function of both compression and saturation to understand the nature of liquid connectivity in saturated pores, and reveals a significant contribution of saturation content on conductive heat transfer in fuel cell DM, which should be accounted for in multiphase modeling effects. The results of this study should be useful to improve predictions of the internal temperature gradients and transport phenomenon inside the PEFCs.

7. Disclaimer

This report was prepared as an account of work sponsored by an agency of the United States Government. Neither the United States Government nor any agency thereof, nor any of their employees, makes any warranty, express or implied, or assumes any legal liability or responsibility for the accuracy, completeness, or usefulness of any information, apparatus, product, or process disclosed, or represents that its use would not infringe privately owned rights. Reference herein to any specific commercial product, process, or service by trade name, trademark, manufacturer, or otherwise does not necessarily constitute or imply its endorsement, recommendation, or favoring by the United States Government or any agency thereof. The views and opinions of authors expressed herein do not necessarily state or reflect those of the United States Government or any agency thereof.

Acknowledgments

This material is based upon work supported by the Department of Energy under Award Number *DE-EE0000470*. The authors' would also like to acknowledge the support of Jon Owejan, Paul Nicotera, Wenbin Gu and General Motors.

References

- [1] S.M. Senn, D. Poulikakos, *J. Power Sources* 130 (2004) 178–191.
- [2] A.Z. Weber, J. Newman, *J. Electrochem. Soc.* 153 (2006) A2205.
- [3] L. Matamoros, D. Brüggemann, *J. Power Sources* 161 (2006) 203–213.
- [4] C. Bao, M. Ouyang, B. Yi, *Int. J. Hydrogen Energy* 31 (2006) 1040–1057.
- [5] A.K. Srouji, M.M. Mench, in: M.M. Mench, E.C. Kumbur, T.N. Veziroglu (Eds.), *Modern Topics in Polymer Electrolyte Fuel Cell Degradation*, Elsevier.
- [6] M. Oszcipok, D. Riemann, U. Kronenwett, M. Kreideweis, M. Zedda, *J. Power Sources* 145 (2005) 407–415.
- [7] S. Kim, M.M. Mench, *J. Power Sources* 174 (2007) 206–220.
- [8] E. Cho, J.-J. Ko, H.Y. Ha, S.-A. Hong, K.-Y. Lee, T.-W. Lim, I.-H. Oh, *J. Electrochem. Soc.* 150 (2003) A1667.
- [9] N. Zamel, E. Litovsky, X. Li, J. Kleiman, *Int. J. Hydrogen Energy* 36 (2011) 12618–12625.
- [10] G.S. Hwang, A.Z. Weber, *J. Electrochem. Soc.* 159 (2012) F683–F692.
- [11] M. Khandelwal, M.M. Mench, *J. Power Sources* 161 (2006) 1106–1115.
- [12] O.S. Burheim, G. Ellila, J.D. Fairweather, A. Labouriau, S. Kjelstrup, J.G. Pharoah, *J. Power Sources* 221 (2013) 356–365.
- [13] O. Burheim, P.J.S. Vie, J.G. Pharoah, S. Kjelstrup, *J. Power Sources* 195 (2010) 249–256.
- [14] G. Karimi, X. Li, P. Teertstra, *Electrochim. Acta* 55 (2010) 1619–1625.
- [15] M.C. Hatzell, A. Turhan, S. Kim, D.S. Hussey, D.L. Jacobson, M.M. Mench, *J. Electrochem. Soc.* 158 (2011) B717.
- [16] M.P. Manahan, M.C. Hatzell, E.C. Kumbur, M.M. Mench, *J. Power Sources* 196 (2011) 5573–5582.
- [17] A. Turhan, S. Kim, M. Hatzell, M.M. Mench, *Electrochim. Acta* 55 (2010) 2734–2745.
- [18] J. Wang, J.K. Carson, M.F. North, D.J. Cleland, *Int. J. Heat Mass Transfer* 49 (2006) 3075–3083.
- [19] J.K. Carson, S.J. Lovatt, D.J. Tanner, A.C. Cleland, *Int. J. Heat Mass Transfer* 48 (2005) 2150–2158.
- [20] J. Yablecki, A. Nabovati, A. Bazylak, *J. Electrochem. Soc.* 159 (2012) B647.
- [21] A. Bazylak, *Int. J. Hydrogen Energy* 34 (2009) 3845–3857.
- [22] J. Yablecki, J. Hinebaugh, A. Bazylak, *J. Electrochem. Soc.* 159 (2012) F805–F809.
- [23] S. Kim, M.M. Mench, *J. Electrochem. Soc.* 156 (2009) B353.
- [24] J.S. Gustavsson, M. Gustavsson, S.E. Gustafsson, *Therm. Conduct.* 24 (1997) 116–122.
- [25] K.T. Cho, M.M. Mench, *J. Power Sources* 195 (2010) 3858–3869.
- [26] J. Ramousse, S. Didierjean, O. Lottin, D. Maillet, *Int. J. Therm. Sci.* 47 (2008) 1–6.
- [27] <http://www.hotdiskinstruments.com/products/instruments-for-thermal-conductivity-measurements/tps-2500-s.html>.
- [28] S.E. Gustafsson, E. Karawacki, M.A. Chohan, *J. Phys. D Appl. Phys.* 19 (1986) 727.
- [29] S.E. Gustafsson, E. Karawacki, M.N. Khan, *J. Phys. D Appl. Phys.* 12 (1979) 1411.
- [30] J. Wang, J.K. Carson, M.F. North, D.J. Cleland, *Int. J. Heat Mass Transfer* 51 (2008) 2389–2397.
- [31] E. Sadeghi, M. Bahrani, N. Djilali, *J. Power Sources* 179 (2008) 200–208.
- [32] J.K. Carson, S.J. Lovatt, D.J. Tanner, A.C. Cleland, *J. Food Eng.* 75 (2006) 297–307.
- [33] S.R. Jagjiwanram, *Appl. Therm. Eng.* 24 (2004) 2727–2735.
- [34] A.Z. Weber, M.A. Hickner, *Electrochim. Acta* 53 (2008) 7668–7674.
- [35] Y. Wang, C.-Y. Wang, *J. Electrochem. Soc.* 153 (2006) A1193.
- [36] M.M. Mench, *Fuel Cell Engines*, John Wiley & Sons, Inc, Hoboken, New Jersey, 2008.
- [37] R.B. Montgomery, *J. Meteorol.* 4 (1947) 193.
- [38] J.P. Owejan, J.E. Owejan, W. Gu, T.A. Trabold, T.W. Tighe, M.F. Mathias, *J. Electrochem. Soc.* 157 (2010) B1456.